Chapter 22
The Zero-Age Main Sequence

We consider here a sequence of chemically homogeneous models in complete (mechanical and thermal) equilibrium with central hydrogen burning. All of them are composed of the same hydrogen-rich mixture, while the stellar mass M varies from model to model along the sequence.

These models can represent very young stars which have just formed from the interstellar medium, and in which the foregoing contraction (see Chap. 28) has raised the central temperature so far that hydrogen burning has started. This provides a long-lasting energy source, and consequently the stars change only on the very long nuclear timescale $\tau_{\rm n}$. Within the much shorter Kelvin–Helmholtz timescale (see Sect. 3.3), the stars will "forget" the details of their thermal history long before the nuclear reactions have noticeably modified the composition. The only nuclear changes that have taken place during the previous phase are the burning of the light elements deuterium, lithium, beryllium and boron in the largest part of the star, and the conversion of carbon to nitrogen in the centre. The latter reactions consume approximately 1 % of the protons in the stellar core; the former ones are orders of magnitude less important due to the very low abundances of the mentioned elements. This is why one can reasonably treat them as homogeneous models in thermal equilibrium. The now-beginning evolution, in which hydrogen is slowly consumed in the stellar core, has such a long duration that most visible stars are presently found in this phase. Our homogeneous models define its very beginning, and their sequence is therefore more precisely called the *zero-age main sequence* (ZAMS), since one usually counts the age of a star from this point on.

22.1 Surface Values

Homogeneous, hydrogen-burning equilibrium models can be very easily calculated and are available for many different chemical compositions. We limit ourselves to discussing a set of calculations with $X_{\rm H} = 0.70$, $X_{\rm He} = 0.28$, such that all heavier

R. Kippenhahn et al., *Stellar Structure and Evolution*, Astronomy and Astrophysics Library, DOI 10.1007/978-3-642-30304-3_22, © Springer-Verlag Berlin Heidelberg 2012

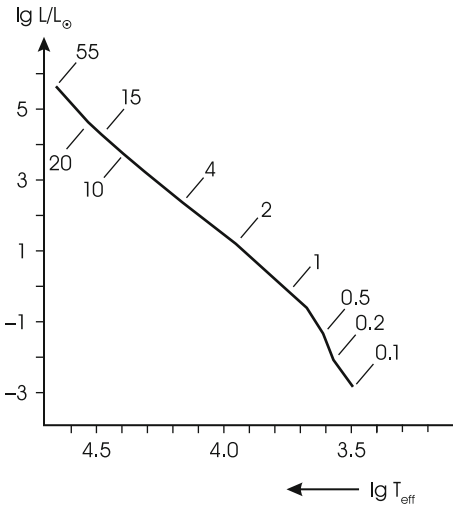

Fig. 22.1
Hertzsprung–Russell diagram with the zero-age main sequence computed for a composition with $X_{\mathrm{H}} = 0.70$, $X_{\mathrm{He}} = 0.28$. The locations of models for several masses between 0.1 and $55 M_{\odot}$ are indicated

elements amount only to 0.02 of the mass.[1] This is a chemical composition typical for the younger population of stars found in the spiral arms of the Milky Way. The metallicity Z is slightly higher than that of the Sun.

Figure 22.1 shows the Hertzsprung–Russell diagram for the models in the wide range of stellar masses from $0.1 M_{\odot}$ to more than $50 M_{\odot}$. L and T_{eff} increase with increasing M, thus forming the ZAMS, which coincides more or less with the lower border of the observed main-sequence band. The slope of the ZAMS below $\approx 0.6\, M_{\odot}$ depends sensitively on the equation of state, the opacities, and the atmospheric boundary conditions.

The important mass-radius and mass-luminosity relations for these models are shown in Figs. 22.2 and 22.3 by the solid lines. In both cases they should constitute a lower envelope to the distribution of stars, since radius as well as luminosity are increasing during the main-sequence evolution and mass remains constant or decreases slightly. Those objects in Fig. 22.2 clearly detached from the bulk of objects are stars that have already developed off the main sequence and therefore have considerably larger radii. Note the very good agreement with theory, although the stars shown do not have identical composition and, in particular, not exactly that of the models. Points below the theoretical sequence may also be due to measurement errors. As predicted already by the simple homology relations for main sequence models [see (20.20) and (20.21)], R increases slowly, and L

[1] Note that we will also use the notation X, Y, and Z for the mass fractions of hydrogen, helium, and the sum of all remaining elements, commonly labelled "metals", as is the case in the astrophysical literature.

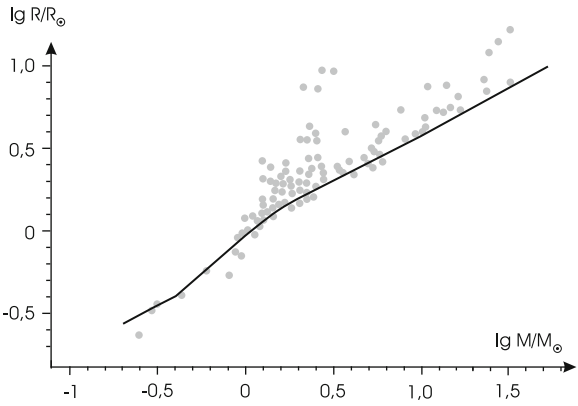

Fig. 22.2 The *line* shows the mass-radius relation for the models of the zero-age main sequence plotted in Fig. 22.1. For comparison, the best measurements (as collected by Malkov et al. 2006, containing the very important catalogue of Andersen 1991) of main sequence primary components of detached and visual binary systems are shown as *grey dots*

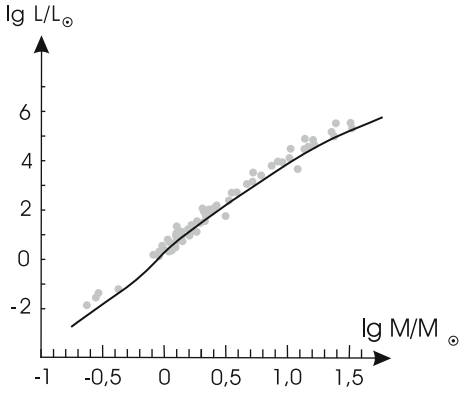

Fig. 22.3 The *line* gives the mass-luminosity relation for the models of the main sequence shown in Fig. 22.1. Measurements of binary systems are plotted for comparison as in Fig. 22.2

increases strongly with increasing M. For an interpolation over a certain range of M we may again write

$$R \sim M^{\xi}, \quad L \sim M^{\eta}\,. \tag{22.1}$$

From the slopes of the curve in Fig. 22.2 we find roughly $\xi = 0.56$ and 0.79 in the upper and lower mass ranges, respectively. In the range of small values of M, there is a pronounced maximum of the slope around $M = 1M_{\odot}$, indicating a remarkable deviation from homologous behaviour in this range. With decreasing effective temperature these models have outer convective zones of strongly increasing extension (cf. Sects. 11.3.2, 11.3.3 and Fig. 22.7). This tends to decrease R, in addition to other effects.

Also the slope of the $M - L$ relation in Fig. 22.3 varies with M. Over the whole mass range plotted, the average of η is about 3.37. For $M = 1 \ldots 10M_{\odot}$ the average exponent is 3.89, while in the larger range $M = 1 \ldots 50M_{\odot}$ it is 3.35. The decreasing slope towards larger M is an effect of the increasing radiation pressure (see below and Sect. 20.2.3).

Let us consider the way in which the variation of the exponents ξ and η influences the slope of the main sequence in the Hertzsprung–Russell diagram. Eliminating M from the two relations (22.1), we find immediately that

$$R \sim L^{\xi/n} \,. \tag{22.2}$$

We introduce this into the relation $L \sim R^2 T_{\rm eff}^4$ and obtain for the main sequence in the Hertzsprung–Russell diagram the proportionality

$$L \sim T_{\rm eff}^{\zeta}, \quad \zeta = \frac{4}{1 - 2\xi/\eta} \,. \tag{22.3}$$

We have seen that for large stellar masses, η decreases and ξ remains about constant with further increasing M. Equation (22.3) then gives an increase of ζ, which means that the main sequence must become gradually steeper towards high luminosities.

We should mention that these two relations belong to the rare instances for which a reasonable quantitative test of the theory is possible. Even here one is rather restricted, since it is extremely difficult to obtain sufficiently precise measurements of R, L, and M. From this point of view, the $M - R$ relation should be the more reliable one. In Figs. 22.2 and 22.3 a selection of the best observed main-sequence double stars are plotted (Andersen 1991; Malkov et al. 2006). When comparing the scattering in the two diagrams one should note that Fig. 22.3 has an appreciably more compressed ordinate. The theoretical curves map out roughly the lower border of the measured values. They would be shifted slightly upwards, for example, by the assumption of a smaller hydrogen content. However, we have compared zero-age main-sequence stars with real stars of varying composition here. In view of the uncertainties and difficulties involved in theory as well as in observation, one can scarcely expect a better fit, particularly when considering the enormous range of values involved (a factor 250 in M, nearly 8 powers of 10 in L).

22.2 Interior Solutions

The behaviour of the interior may be illustrated by characteristic variables as functions of m/M. They are plotted in Fig. 22.4 for two stellar masses in order to demonstrate typical dependencies of the solutions on M.

The density ϱ (Fig. 22.4a) increases appreciably towards the centre where we have $\varrho_{\rm c} \approx 10^2\,{\rm g\,cm^{-3}}$ for 1 $M_\odot$, i.e. roughly a factor 10^9 larger than in the photosphere. For $10 M_\odot$, the central density is smaller by more than a factor 10. The inward increase of ϱ indicates a very strong concentration of the mass elements towards the centre, illustrated in Fig. 22.4b. For 1 $M_\odot$, the inner 30 % of the radius (i.e. only 3 % of the total volume) contains 50 % of the mass; and in the outer 50 % of R (i.e. 88 % of the volume) only about 15 % of M can be found.

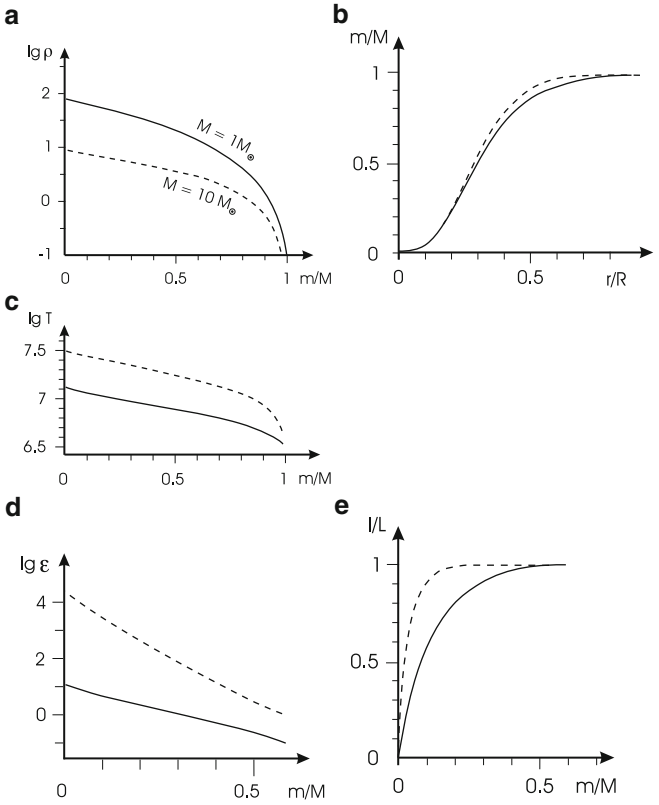

Fig. 22.4 The run of some functions inside zero-age main-sequence models for $M = 1M_\odot$ (*solid lines*) and $M = 10M_\odot$ (*dashed lines*) with the same composition as in Fig. 22.1 ($X_\mathrm{H} = 0.70, X_\mathrm{He} = 0.28$); (**a**) density ϱ (in $\mathrm{g\,cm^{-3}}$), (**b**) radial mass distribution $m(r)/M$, (**c**) temperature T (in K), (**d**) nuclear energy production (in erg $\mathrm{g^{-1}\ s^{-1}}$), (**e**) local luminosity l

The temperature (Fig. 22.4c) also increases towards the centre. For 1 $M_\odot$, the central value of 1.36×10^7 K is a factor 2,400 larger than the photospheric value. Values of $T > 3 \times 10^6$ K extend to $m \approx 0.95M$, so that the average T value (averaged over the mass elements) is roughly 7.7×10^6 K. In a $10M_\odot$ star, T has slightly more than twice the values of corresponding mass elements for 1 $M_\odot$.

The behaviour of T is necessarily reflected by that of the rate of energy generation due to hydrogen burning (Fig. 22.4d). The dependence of ε on T (cf. Sect. 18.5.1), together with the T gradient, yields a strong decrease of ε from the centre outwards. In the $1M_\odot$ star, ε has dropped by a factor 10^2 from the centre to $m = 0.6M$, and still further outward it is quite negligible. This is particularly well seen in Fig. 22.4e: 90 % of L is generated in the inner 30 % of M; and l reaches about 99 % of L at $m/M = 0.53$. In the central part of the $10M_\odot$ star, where

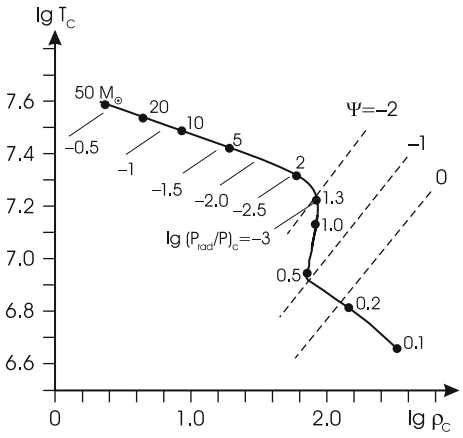

Fig. 22.5 The *heavy solid line* gives the central temperature T_c (in K) over the central density ϱ_c (in $\mathrm{g\,cm^{-3}}$) for the same zero-age main-sequence models as in Fig. 22.1. The *dots* give the positions of some models with masses between $M = 0.10$ and $M = 50$ (in solar masses). The *labels* below the curve indicate the logarithmic fractional contribution of the radiation pressure P_{rad} to the total pressure in the centre. The *dashed lines* give the constant degeneracy parameter ψ of the electron gas

$T_c = 3 \times 10^7$ K, the dominant energy source is the CNO cycle (instead of the *pp* chain in $1M_\odot$). The much larger T dependence of ε gives an even more pronounced concentration of ε towards the centre (Fig. 22.4d). In the innermost 30 % of M, ε drops by about a factor 10^3 (as compared to a factor 10 in the same interval of $1M_\odot$). This corresponds to an ε with an exponent of T roughly three times larger. Further outwards, where T is low enough for the *pp* chain to dominate, the slope of ε becomes the same in both stars. In the $10M_\odot$ star, 90 % of the total luminosity is generated within the innermost 10 % of the mass (Fig. 22.4e).

We have seen that in spite of all similarities there are characteristic differences between the interior solutions for different values of M. Some of these can be found in the plot of the central values of temperature and density (Fig. 22.5). This diagram exhibits at least qualitatively another prediction of the homology considerations in Chap. 20: with increasing M, there is a slight increase of T_c together with a substantial decrease of ϱ_c. Between $M = 2M_\odot$ and $50M_\odot$ the differences are $\Delta \lg T_c = +0.28$ and $\Delta \lg \varrho_c = -1.43$. The striking change of the curve around $1.3M_\odot$ is a direct consequence of the transition from the CNO cycle to the *pp*-chains as the dominating energy source. At $M = 1.4M_\odot$, the CNO cylce dominates at the centre, which reaches the critical temperature of $\lg T_c = 7.25$ (Fig. 18.8), while at $M = 1.9M_\odot$ the *pp*-contribution to the total energy production has fallen below 50 % (see also Fig. 22.6). From the homology relations (20.25) and Table 20.1 the slope of the curve in Fig. 22.5 can be predicted: it has a small negative value at

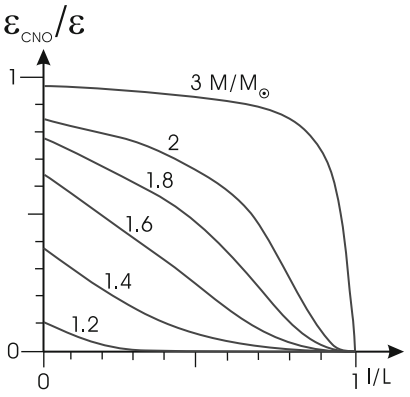

Fig. 22.6 For six zero-age main-sequence models of the same composition as in Fig. 22.1 (mass in solar units indicated along each curve), the fraction that the CNO cycle contributes to the total energy generation rate at different places inside the model (characterized by the corresponding local luminosity l at the abscissa) is shown

the high mass end (-0.16 compared to -0.20 from the numbers given above) and a large negative value ($\lesssim -2$) for $M < 1.3 M_\odot$. In addition, there are deviations from homology, partly due to the appearance of the outer convective zone (the homology relations were derived under the assumption of radiative energy transport), which is deepening with decreasing mass. The extension of convective regions should certainly influence the centre, since they have a less pronounced mass concentration than radiative regions. Note that both flat parts of the $T_c - \varrho_c$ curve in Fig. 22.5 belong to models in which the central part is convective (cf. Fig. 22.7). At the lowest masses the stars are fully convective and follow the relations for a polytrope of index $n = 3/2$ (Chap. 19 and Sect. 24.2).

In the upper range of masses degeneracy is negligible, while it becomes increasingly important towards smaller M owing to the increasing density. Below $0.5 M_\odot$, say, other deviations from the ideal gas approximation also become important in the equation of state, for example, electrostatic interaction between the ions.

On the other hand, the radiation pressure $P_{\rm rad}$ must increase towards larger M owing to the increasing T, since $P_{\rm rad} \sim T^4$. At $M = 1 M_\odot$, radiation contributes only the negligible fraction of a few 10^{-4} to the total central pressure. This fraction becomes about 1 % at $4 M_\odot$, while in the centre of the $50 M_\odot$ star, $P_{\rm rad}$ contributes no less than 1/3 to the total pressure (see Fig. 22.5).

Another effect of the growing T_c, which also occurs around 1 $M_\odot$, is the transition from the *pp* chain to the CNO cycle as the dominant energy source (compare also Fig. 18.8). For models in the transition region from $M = 1\ M_\odot$ to 3 $M_\odot$, Fig. 22.6 shows the contribution of $\varepsilon_{\rm CNO}$ to the local energy generation rate as a function of l/L. The integral over such a curve gives the fraction of L due to burning in the CNO cycle. This amounts only to a few percent for $M = 1.2\ M_\odot$. In the 1.6 $M_\odot$ star, the CNO cycle already contributes 65 % at the centre, and nearly one half of the total luminosity. It clearly dominates the whole energy generation for $1.8 M_\odot$ and more massive stars.

22.3 Convective Regions

Knowledge of the extension of convective regions is very important in view of their influence on the ensuing chemical evolution. A rough overview can be obtained from Fig. 22.7, where m/M and $\lg M/M_\odot$ are ordinate and abscissa. For any given stellar mass M along a line parallel to the ordinate it is indicated what conditions we would encounter when drilling a radial borehole from the surface to the centre. In particular, one can see whether the corresponding mass elements are convective or radiative. Aside from the stars of smallest mass ($M < 0.25M_\odot$), we can roughly distinguish between two types of model:

convective core + radiative envelope (upper main sequence);

radiative core + convective envelope (lower main sequence).

The transition from one type to the other again occurs near $M = 1M_\odot$.

The distinction between convective and radiative regions is made here by using the Schwarzschild criterion (see Sect. 6.1), which predicts convection if the radiative gradient of temperature $\nabla_{\rm rad}$ exceeds the adiabatic gradient $\nabla_{\rm ad}$ (The gradient ∇_μ of the molecular weight appearing in the Ledoux criterion is zero in these homogeneous models. Possible effects of overshooting will be discussed in Chap. 30.). The variation of these gradients (together with that of the actual gradient ∇) throughout the star is plotted in Fig. 22.8 for $M = 1M_\odot$ and $10M_\odot$. For the abscissa, $\lg T$ is chosen, since this conveniently stretches the scale in the complicated outer layers.

Let us start with the simpler situation concerning the convective core. When comparing Fig. 22.8a, b, we see that the convective core in the more massive models is caused by a steep increase of $\nabla_{\rm rad}$ towards the centre. The reason for this is that the dominating CNO cycle , with its extreme temperature sensitivity, concentrates the energy production very much towards the centre (cf. the curve $l/L = 0.5$ in Fig. 22.7, and Fig. 22.4e). Therefore we find in these stars very high fluxes of energy ($l/4\pi r^2$) at small r, which produce large values of $\nabla_{\rm rad}$. Figure 22.7 shows a remarkable increase in the extent of the convective core for increasing M. The core covers as much as 65 % of the stellar mass in a star of $50M_\odot$, an increase caused by the increasing radiation pressure (cf. Sect. 22.2 and Fig. 22.5), which depresses the value of $\nabla_{\rm ad}$ well below its standard value of 0.4 for an ideal monatomic gas [see (13.12)]. In the centre of the $50M_\odot$ model, roughly 1/3 of P is radiation pressure, and $\nabla_{\rm ad} \approx 0.27$. From Fig. 22.8b it is clear that a depression of $\nabla_{\rm ad}$ in the central region will shift the intersection with $\nabla_{\rm rad}$ (i.e. the border of the convective core) outwards to smaller T. When we increase M to much larger values still, the top of the convective core will finally approach the surface such that we should obtain fully convective stars. We then approach models of the so-called supermassive stars (see Sect. 19.10).

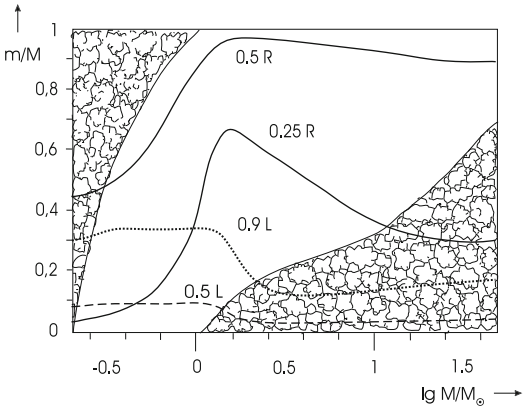

Fig. 22.7 The mass values m from centre to surface are plotted against the stellar mass M for the same zero-age main-sequence models as in Fig. 22.1. "Cloudy" areas indicate the extension of convective zones inside the models. Two *solid lines* give the m values at which r is 1/4 and 1/2 the total radius R. The *dashed and dotted lines* show the mass elements inside which 50 % and 90 % of the total luminosity L are produced

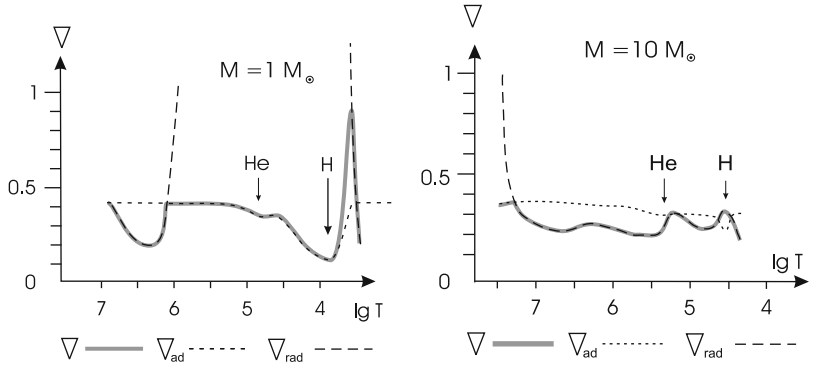

Fig. 22.8 The *grey solid lines* show the actual temperature gradient $\nabla = d \ln T / d \ln P$ over the temperature T (in K) inside two zero-age main-sequence models of $1 M_\odot$ (*left panel*) and $10 M_\odot$ (*right panel*). The corresponding adiabatic gradients ∇_{ad} (*dotted lines*) and radiative gradients ∇_{rad} (*dashed lines*) are also plotted, and the location of the ionization zones of hydrogen and helium are indicated (*arrows*). The chemical composition of the models is the same as for those of Fig. 22.1

In less massive stars, the *pp* chain with its smaller temperature sensitivity dominates. This distributes the energy production over a much larger area, so that the flux and ∇_{rad} are much smaller in the central region, which thus remains radiative.

Outer convective envelopes can generally be expected to occur in stars of low effective temperature, as the discussion of the boundary conditions in Sect. 11.3.2 has already shown. When studying the different gradients in the outer layers of cool stars (Fig. 22.8a), one finds a variety of complicated details. The variation of ∇_{ad} clearly shows depressions in those regions where the most abundant

elements, hydrogen ($T \gtrsim 10^4$ K) and helium ($T \approx 10^5$ K), are partially ionized (see Chap. 14). The most striking feature is that $\nabla_{\rm rad}$ reaches enormous values (more than 10^5). This is due to the large opacity κ, which here increases by several powers of 10 (cf. Chap. 17). Therefore the Schwarzschild criterion indicates convective instability: the models have an outer convective zone. In the largest part of it, the density is so high that convection is very effective and the actual gradient ∇ is close to $\nabla_{\rm ad}$. Convective transport becomes ineffective only in the outermost, superadiabatic part, where ∇ is clearly above $\nabla_{\rm ad}$. Scarcely anything of all these features appears in the hot envelope of the $10M_\odot$ star (Fig. 22.8b). $\nabla_{\rm rad}$ remains nearly at the same level; even the photosphere is too hot for hydrogen to be neutral, and only the small dip from the second He ionization is seen immediately below the photosphere. This causes such a shallow zone with convective instability that only for special cases, depending on the detailed chemical composition, convective motions set it.

The outer convection zone gradually penetrates deeper into the star with decreasing $T_{\rm eff}$. Its lower border finally reaches the centre at $M \lesssim 0.25M_\odot$ (left end of Fig. 22.7), such that the main-sequence stars of even smaller masses are fully convective.

22.4 Extreme Values of M

The ZAMS ends at extreme low and high mass values. Only in recent years detailed calculations for main-sequence stars of very low M have become available. The difficulties of modelling them lie in particular in the fact that the input physics is complicated and the available data not very reliable. This concerns the notorious problem of the treatment of convection, as well as the opacity values for mixtures containing many molecules. Both these effects are important in very cool envelopes. Complications for the interior structure are equally severe. They arise, for example, from the difficult treatment of particle interaction in the low-temperature high-density regime and influence the equation of state and the electron screening of nuclear reactions. Progress has been made in the equation of state under such conditions (Sect. 16.6), in the treatment of the opacities (Sect. 17.8) and the calculation of the atmospheric structure. The latter is very important since stars below $\approx 0.2M_\odot$ are fully convective (Fig. 22.7) and their interior structure therefore depends very much on the outer boundary conditions (Fig. 11.2).

Quite another problem concerns the relevance of the calculated equilibrium models for real, evolving stars. At the low central temperatures in models of extremely small masses, for example, the time for reaching equilibrium burning can become exceedingly long. A preceding phase in which the original ^{3}He is burned may be at least equally important, but this ^{3}He content is very uncertain. And below about $M = 0.1M_\odot$, even the original contraction leads so far into electron degeneracy that hydrogen burning is no longer ignited (refer to Chap. 28).

In this sense one may speak of the "lower end of the main sequence" at this mass value. Disregarding this evolutionary argument, however, one can ask whether solutions for main-sequence models (homogeneous, hydrogen burning, complete equilibrium) exist down to arbitrary small values of M. It turns out that such models end to exist at $M \approx 0.08 M_\odot$. Real stars simply fail to provide all the luminosity from nuclear burning alone and need thermal energies to supply the rest of the energy. Such objects are called *brown dwarfs* and are no longer considered as "real stars". Details about very low-mass stars and brown dwarfs, their physical properties and how they are modelled, can be found in the review by Chabrier and Baraffe (2000). Although they are extremely faint, they are now routinely found with large telescopes. A decisive test to confirm that a "star" is indeed a brown dwarf is the *lithium test*: going down in mass along the main sequence, stars become fully convective. Any change in element abundances due to hydrogen burning is therefore reflected in the surface abundances. This includes lithium, which, as part of the *pp2* chain (18.62), is destroyed due to proton captures at temperatures above $\approx 2.5 \times 10^6$ K. Its surface abundance is therefore very low on the lower main sequence, as it is almost completely destroyed throughout the star. If the mass is however low enough such that the critical temperature is not reached even at the centre, lithium can survive and "reappears" for the very faintest main-sequence stars. The mass at which such low central temperatures are reached is $\approx 0.06 M_\odot$, which is lower than the $0.08\, M_\odot$, which denotes the transition from stars to brown dwarfs. The lithium test has lead to the first definite detection of brown dwarfs.

In the direction towards large M, on the other hand, the sequence of equilibrium models can principally be continued up to the "supermassive" stars (see Sect. 19.10). Long before they are reached, however, an instability occurs which sets in between $M \approx 60$ and $100 M_\odot$ (depending on the composition). It is a vibrational instability caused by the so-called ε mechanism (see Sect. 41.5) and supported by the large amount of radiation pressure. Such stars, instead of sitting quietly at their proper place on the main sequence, will start to oscillate with growing amplitude. This may go so far as to throw off matter from the surface, until the mass is reduced below the critical value for the instability.

22.5 The Eddington Luminosity

For massive, hot stars there exists another physical limit for hydrostatic stability, which results from the increasingly important radiation pressure. According to (13.1)

$$P_{\mathrm{rad}} = \frac{1}{3} U = \frac{a}{3} T^4 \, .$$

Therefore there exists a gradient of the radiation pressure

$$\frac{dP_{\mathrm{rad}}}{dr} = \frac{a}{3} T^3 \frac{dT}{dr} \, , \tag{22.4}$$

which exerts, just like the gas pressure gradient, an outward acceleration ($dP_{\rm rad}/dr < 0$)

$$g_{\rm rad} = -\frac{1}{\rho}\frac{dP_{\rm rad}}{dr} \ . \tag{22.5}$$

(This outward force is already included in the hydrostatic equation, if the total pressure is considered according to (13.2). Here we consider it separately only for clarifying the effect.)

Using (5.8) we see that we can rewrite (22.5) as

$$g_{\rm rad} = \frac{\kappa F_{\rm rad}}{c} = \frac{\kappa L_r}{4\pi r^2 c} \ . \tag{22.6}$$

In case that radiation pressure completely dominates over gas pressure, a star can no longer be in hydrostatic equilibrium if $g_{\rm rad} > -g$. The sum of both accelerations can be written as

$$g + g_{\rm rad} = -\frac{Gm}{r^2}\left[1 - \frac{\kappa L_r}{4\pi cGm}\right] = -\frac{Gm}{r^2}\left[1 - \Gamma_r\right] \ , \tag{22.7}$$

where Γ_r can be understood as the ratio of the luminosity relative to the critical luminosity at which the bracket changes sign, and thus the star becomes unbound. For $m = M$ this critical luminosity is called the *Eddington luminosity* and is

$$L_{\rm E} = \frac{4\pi cGM}{\kappa} \ . \tag{22.8}$$

Expressed in solar units it is

$$\frac{L_{\rm E}}{L_\odot} = 1.3 \times 10^4 \frac{1}{\kappa}\frac{M}{M_\odot} \tag{22.9}$$

and grows linearly with stellar mass. Since $L \sim M^3$, stars obviously reach a limit, where radiation pressure is able to drive a strong stellar wind, and which depends on the opacity.

For hot, massive stars electron scattering is the dominating opacity source, which can be approximated by (17.1), and is $\kappa_{\rm sc} = 0.20(1 + X)$. For a mass fraction of hydrogen of 0.70 (22.9) simplifies to

$$\frac{L_{\rm E}}{L_\odot} = 3.824 \times 10^4 \frac{M}{M_\odot}. \tag{22.10}$$

For $M \approx 200\, M_\odot$ the luminosity of massive main-sequence stars reach the Eddington limit and disperse. This is a rough estimate for an upper limit. In reality the instability of the ε mechanism occurs at lower mass. However, the Eddington limit can become quite important in other situations.